

Generating three transparency windows, Fano-resonance, and slow/fast light in magnomechanical system through an auxiliary microwave cavity

M'bark Amghar, Noura Chabar, Amjad Sohail, and Mohamed Amazioug

Citation: Chin. Phys. B, 2026, 35 (**5**): 050306. DOI: 10.1088/1674-1056/ae1c2f
http://cpb.iphy.ac.cn; http://iopscience.iop.org/cpb

What follows is a list of articles you may be interested in

Measurement-device-independent quantum key distribution with entanglement-assisted linear Bell state measurement

Cheng Zhang(张诚), Cheng Liu(刘成), Jiawei Ying(应佳伟), Shipu Gu(顾世浦), Lan Zhou(周澜), Yin Ma(马寅), Kang Gao(高亢), Hai Wei(魏海), Kai Wen(文凯), and Yubo Sheng(盛宇波)
Chin. Phys. B, 2026, 35 (**4**): 040310. DOI: 10.1088/1674-1056/ae3605

Asymmetric model of the dynamic quantum Cournot duopoly game with asymmetric information and heterogeneous players

Huaxin Chen(陈华鑫) and Wensheng Jia(贾文生)
Chin. Phys. B, 2026, 35 (**4**): 040307. DOI: 10.1088/1674-1056/ae00af

Analysis of urban atmospheric influence on free-space quantum key distribution

Hai-Long Zhang(张海龙), Xing-Ran Chen(陈星燃), and Tan Li(李坦)
Chin. Phys. B, 2026, 35 (**4**): 040306. DOI: 10.1088/1674-1056/ae0bfc

Tunable phonon-photon coupling induces double magnomechanically induced transparency and enhances slow light in an atom-opto-magnomechanical system

M'bark Amghar, Noura Chabar, and Mohamed Amazioug
Chin. Phys. B, 2024, 33 (**12**): 120308. DOI: 10.1088/1674-1056/ad8cbb

Floquet scattering through a parity-time symmetric oscillating potential

Xuzhen Cao(曹序桢), Zhaoxin Liang(梁兆新), and Ying Hu(胡颖)
Chin. Phys. B, 2023, 32 (**3**): 030302. DOI: 10.1088/1674-1056/aca39a

---

Generating three transparency windows, Fano-resonance, and slow/fast light in magnomechanical system through an auxiliary microwave cavity

M'bark Amghar[1], Noura Chabar[1], Amjad Sohail[2,3], and Mohamed Amazioug[1,†]

[1] *LPTHE-Department of Physics, Faculty of sciences, Ibnou Zohr University, Agadir, Morocco*
[2] *Department of Physics, Government College University, Allama Iqbal Road, Faisalabad* 38000, *Pakistan*
[3] *Instituto de Física Gleb Wataghin, Universidade Estadual de Campinas, Campinas, SP, Brazil*

(Received 4 September 2025; revised manuscript received 20 October 2025; accepted manuscript online 6 November 2025)

In this paper, we propose a theoretical scheme to investigate the magnomechanically induced transparency (MMIT) phenomenon, Fano resonances, and slow/fast light effects in a hybrid cavity magnomechanical system. The magnomechanical system consists of two cavities: the principal cavity contains two ferromagnetic yttrium iron garnet (YIG) spheres, and the auxiliary cavity contains an atomic assembly. These two cavities are connected via photon tunneling, with the principal cavity being driven by two electromagnetic fields. The photon-magnon and phonon-magnon couplings are responsible for the magnon-induced transparency (MIT) and MMIT observed in the probe output spectrum. Furthermore, we examine the impacts of tunneling coupling, atom-photon coupling, and the magnetic field on the absorption, dispersion, and transmission spectra. We provide an explanation of the mechanism behind the Fano resonance phenomenon. Additionally, we address the phenomenon of slow and fast light propagation. Moreover, we demonstrate that the group delay of the probe field can be enhanced by increasing the photon tunneling strength. We also show that the slow light profile is reduced by adjusting the atom-photon coupling strength. This model is experimentally feasible, and we anticipate that these findings have potential applications in quantum information processing and communication.

Keywords: magnomechanical system, magnomechanically induced transparency, auxiliary cavity, Fano resonance, slow and fast light

PACS: 03.67.–a, 03.75.Lm

DOI: 10.1088/1674-1056/ae1c2f **CSTR:** 32038.14.CPB.ae1c2f

1. Introduction

Electromagnetically induced transparency (EIT)[1–4] is a quantum interference phenomenon observed in multi-level atomic systems. It arises when these systems are subjected to intense laser fields, resulting in the suppression of absorption for a weak probe light. Initially predicted by Harris *et al.*[2] and experimentally demonstrated by Boller *et al.*[3] using strontium vapor, EIT has become a widely researched phenomenon. This research has unveiled various novel occurrences, such as quantum memories for photons,[5,6] slow light,[7,8] enhanced nonlinearity,[9] vibrational cooling,[10] optical switches,[11] and multiple EITs with two or more transparency windows.[12–16] Typically, multiple EITs arise in systems with coherent multi-channels, enabling prolonged nonlinear interactions between weak fields, and have been proposed as a method to coherently control photon-photon interactions.[17]

Optomechanically induced transparency (OMIT), a phenomenon analogous to EIT, was first explored in 2010 by Weis *et al.*[10] within vibrational cavity optomechanical systems. This effect emerges due to destructive interference among various internal field pathways in the system, creating a transparency window for probe light in spectral regions that would typically exhibit strong absorption.[18] This phenomenon has been proposed for use in various applications, including ultra-slow light propagation,[19] quantum routers,[20] precision measurement,[21] and four-wave mixing.[22] So far, the emergence of various new cavity optomechanical systems has led to theoretical research on the multiple-OMIT phenomenon. This research includes multiple-resonator optomechanical systems,[23] hybrid piezo-optomechanical cavity systems[24,25] and atomic-media-assisted optomechanical systems,[26,27] single-photon emitters,[28] Bose–Einstein condensates,[29] and nonlinear optomechanical systems,[30] among others.

Recently, the cavity magnonic system (CMS) featuring a yttrium iron garnet (YIG) sphere has garnered significant interest, similar to the field of cavity optomechanics. This system offers numerous advantages over traditional systems due to the unique properties of magnetic materials, such as low damping rates, high spin density, and strong cooperativity with microwave photons.[31–36] These characteristics make CMS an ideal platform for studying strong light-matter interactions. Moreover, magnons have excel-

†Corresponding author. E-mail: m.amazioug@uiz.ac.ma

© 2026 Chinese Physical Society and IOP Publishing Ltd. All rights, including for text and data mining, AI training, and similar technologies, are reserved.

lent coupling capabilities with various quantum systems, including optical photons, microwaves,[37] optical whispering gallery modes (WGMs),[38] superconducting qubits,[39] and phonons.[40] Due to these characteristics, YIG systems are employed to investigate a variety of coherent phenomena similar to those observed in optomechanical systems. These phenomena include ground-state cooling of magnomechanical resonators,[41] quantum entanglement,[42–45] magnomechanically induced transparency (MMIT),[46–49] as well as the engineering of slow and fast light,[48–52] and the phenomena of bistability and nonreciprocity.[53,54]

In their CMS research, Ullah *et al.*[49] explored various intriguing quantum effects by exploiting the nonlinearity of magnetostrictive interactions in a system of two ferromagnetic YIG spheres coupled to a single microwave cavity mode. They demonstrated MMIT and magnon-induced transparency (MIT).[48,49,55] In addition, they observed the emergence of Fano resonance in the probe field.[56–58] They also reported slow and fast light propagation. Liao *et al.*[48] studied MMIT as well as slow and fast light effects in a system comprising a high-quality YIG sphere and an atomic ensemble, both located inside a microwave cavity. Recently, Liu *et al.*[59] suggested a scheme for an auxiliary-microwave-assisted coupled magnomechanical model (AMCA) involving two YIG spheres. They introduced a mechanism for simultaneously enhancing quantum cooling and entanglement by coupling an auxiliary microwave cavity to a magnomechanical cavity.

In this paper, we investigate the MMIT phenomenon, Fano resonance, transmission, and slow and fast light effects in a magnomechanical system, which consists of two single cavities connected by single-photon hopping and includes an atomic ensemble and two YIG spheres (see Fig. 1). We investigate the effect of the photon hopping coupling strength, atom-photon coupling strength, and the magnetic field on the absorption and dispersion spectra. Moreover, we study Fano resonances in the output probe field. Additionally, we explore slow and fast light propagation, clarifying that the group delay is influenced by the tunability of the photon hopping coupling strength, as well as the atom-photon coupling.

The organization of this paper is delineated as follows: Section 2 introduces the system, presents the formula for its Hamiltonian, and outlines the relevant quantum Langevin equations (QLEs) while calculating the output field. In Section 3, we examine magnomechanically induced transparency and analyze how the photon hopping coupling strength f, atom-photon coupling strength, and magnetic field affect the input spectrum. Section 4 focuses on the study of Fano resonance in the output field. Section 5 describes the transmission of the probe field and evaluates the group delays related to slow and fast light propagation. In Section 6, we examine the feasibility of our system using current experimental parameters and configurations. Finally, the paper concludes with concluding remarks.

2. Model

In the hybrid coupled-cavity magnomechanical system depicted in Fig. 1, we consider two single-mode cavities connected by single-photon hopping f, each with resonance frequencies ω_r $(r = 1, 2)$, including an atomic ensemble and two YIG spheres. This interconnected system includes six excitation modes: microwave electromagnetic modes in cavity A and cavity B, phonon and two magnon modes in the YIG sphere, and atomic excitation within cavity B.

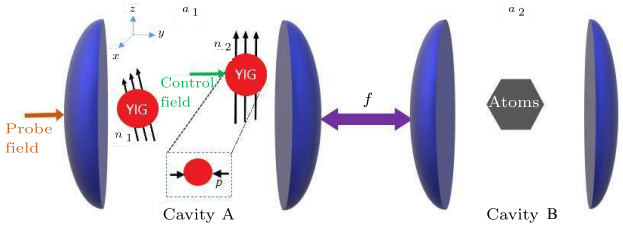


Fig. 1. A schematic representation of two single-mode cavities, designated as A and B, which are interconnected with a coupling strength denoted by f. Cavity A encompasses two YIG spheres and is driven by an external laser field (probe field) operating at a frequency $\omega_{\rm d}$. Each sphere is positioned within a uniform bias magnetic field and near the peak magnetic field of the magnomechanical cavity, facilitating the interaction between the photon mode a_1 and the two magnon modes, n_1 and n_2. The right sphere is directly affected by an external microwave field oriented along the y-direction, which functions as a control field in our model. Cavity B houses an ensemble of N two-level atoms, each with an intrinsic frequency ω_u.

In cavity A, each sphere is subjected to a uniform magnetic field along the z-direction, which excites magnonic modes. These modes are coupled to the cavity A field via dipolar magnetic interactions. Excitation of the magnonic modes inside a sphere results in fluctuating magnetization, which in turn induces changes in the lattice structure. The magnetostrictive force generates vibrations in the YIG spheres, leading to interactions between magnons and phonons within these spheres. The strength of the single-magnon magnomechanical coupling is notably weak[57] and depends on both the diameter of the sphere and the orientation of the external polarization field. By considering a larger n_1 sphere, or by changing the orientation of the polarizing magnetic field applied to it, the magnomechanical coupling of this sphere can be neglected.[45] In this context, we assume that the orientation of the polarizing field on the n_1 sphere is configured so that the single-magnon magnomechanical interaction is extremely weak and can be ignored.[57] Nevertheless, the magnomechanical interaction of the n_2 sphere is significantly enhanced by the direct excitation of its magnon mode through an external microwave actuator. This microwave driver functions as the control field within our model. Furthermore, cavity A is driven by a weak probe field.

Within cavity B, an ensemble comprising N two-level atoms, characterized by a transition frequency ω_u, interacts

with the cavity field. Each atom in the ensemble is described by spin-1/2 Pauli matrices σ_+, σ_-, and σ_z. The collective spin operators associated with atomic polarization are represented as $S_{+,-,z} = \sum_{i=1}^{N} \sigma^i_{+,-,z}$. These operators satisfy the commutation relations: $[S_+, S_-] = S_z$ and $[S_z, S_\pm] = \pm 2 S_\pm$.[60,61] The operators $S_\pm$ and S_z can be expressed in terms of bosonic annihilation and creation operators u and $u^\dagger$ via the Holstein-Primakoff transformation[61–64]

$$S_+ = u^\dagger \sqrt{N - u^\dagger u} \approx u^\dagger \sqrt{N}, S_- = u\sqrt{N - u^\dagger u} \approx u\sqrt{N},$$
$$S_z = u^\dagger u - \frac{N}{2},$$

where $[u, u^\dagger] = 1$. This transformation is valid under the condition that the population of atoms in the ground state greatly exceeds that in the excited state, ensuring $S_z \approx \langle S_z \rangle \approx -N$.[65]

We model the system using high-purity YIG spheres of 250 μm in diameter, containing ferric ions (Fe^{3+}) with a number density $\rho = 4.22 \times 10^{27}$ m^{-3}. The corresponding total spin is $S = \frac{5}{2}\rho \mathcal{V} = 7.07 \times 10^{14}$, where $\mathcal{V}$ is the YIG volume. The collective spin operator S satisfies the standard commutation relations $[S_\alpha, S_\beta] = \mathrm{i}\varepsilon_{\alpha\beta\gamma} S_\gamma$. The complete Hamiltonian characterizing the system is

$$\begin{aligned} H/\hbar =& \sum_{r=1}^{2} \omega_r a_r^\dagger a_r + \omega_u u^\dagger u + \sum_{r=1}^{2} \omega_{n_r} n_r^\dagger n_r + \omega_\mathrm{p} p^\dagger p \\ &+ g_{np} n_2^\dagger n_2 \left(p + p^\dagger\right) + f\left(a_1^\dagger a_2 + a_1 a_2^\dagger\right) \\ &+ G_{au}\left(u a_2^\dagger + u^\dagger a_2\right) + \sum_{r=1}^{2} g_r \left(a_1 n_r^\dagger + a_1^\dagger n_r\right) \\ &+ \mathrm{i}\left(a_1^\dagger \varepsilon_\mathrm{d} \mathrm{e}^{-\mathrm{i}\omega_\mathrm{d} t} - a_1 \varepsilon_\mathrm{d}^* \mathrm{e}^{\mathrm{i}\omega_\mathrm{d} t}\right) \\ &+ \mathrm{i}\Omega\left(n_2^\dagger \mathrm{e}^{-\mathrm{i}\omega_0 t} - n_2 \mathrm{e}^{\mathrm{i}\omega_0 t}\right). \end{aligned} \tag{1}$$

The first four terms of Eq. (1) represent the energies of cavities A and B, atomic excitation, magnon (n_1 and n_2) modes, and the phonon mode. Here, ω_r are the cavity resonance frequencies, ω_u is the atomic transition frequency, ω_{n_r} are the magnon frequencies, and ω_p is the phonon frequency. Notably, $\omega_{n_r} = \gamma H_r$ can be tuned via the external bias magnetic field H_r. The operators $a_r(a_r^\dagger)$, $u(u^\dagger)$, $n_r(n_r^\dagger)$, and $p(p^\dagger)$ satisfy canonical commutation relations: $[a_r, a_r^\dagger] = 1$, $[u, u^\dagger] = 1$, $[n_r, n_r^\dagger] = 1$, and $[p, p^\dagger] = 1$.

The next four terms describe intersystem couplings: magnon-phonon (g_{np}), cavity-cavity (f), atom-cavity (G_{au}), and cavity-magnon (g_r). The collective atom-cavity coupling is $G_{au} = h\sqrt{N}$, where $h = \nu\sqrt{\omega_2/(2\hbar\varepsilon_0 V)}$, ν is the atomic dipole moment, V is the cavity volume, and ε_0 is the permittivity of free space. The penultimate term represents a probe field driving cavity A, with amplitude $\varepsilon_\mathrm{d} = \sqrt{2\kappa_a P_\mathrm{d}/(\hbar\omega_\mathrm{d})}$ and frequency ω_d. The last term describes a microwave drive on the magnon mode n_2 with Rabi frequency $\Omega = \frac{\sqrt{5}}{4}\gamma\sqrt{N}B$, where B is the drive amplitude and $\gamma = 28$ GHz/T is the gyromagnetic ratio.[66]

In Eq. (1), we neglect the nonlinear term $K n_r^\dagger n_r^\dagger n_r n_r$, which could arise from strongly driven magnon modes.[54] This is justified if $K|\langle n_2 \rangle|^3 \ll \Omega$, which holds for the parameters considered here. In the rotating frame of the drive frequency ω_0 and within the rotating-wave approximation, the Hamiltonian becomes

$$\begin{aligned} H/\hbar =& \sum_{r=1}^{2} \Delta_r a_r^\dagger a_r + \Delta_u u^\dagger u + \sum_{r=1}^{2} \Delta_{n_r} n_r^\dagger n_r + \omega_\mathrm{p} p^\dagger p \\ &+ g_{np} n_2^\dagger n_2 (p + p^\dagger) + f(a_1^\dagger a_2 + a_1 a_2^\dagger) \\ &+ G_{au}(u a_2^\dagger + u^\dagger a_2) + \sum_{r=1}^{2} g_r (a_1 n_r^\dagger + a_1^\dagger n_r) \\ &+ \mathrm{i}(a_1^\dagger \varepsilon_\mathrm{d} \mathrm{e}^{-\mathrm{i}\delta t} - a_1 \varepsilon_\mathrm{d}^* \mathrm{e}^{\mathrm{i}\delta t}) + \mathrm{i}\Omega(n_2^\dagger - n_2), \end{aligned} \tag{2}$$

where $\Delta_r = \omega_r - \omega_0$, $\Delta_u = \omega_u - \omega_0$, $\Delta_{n_r} = \omega_{n_r} - \omega_0$, and $\delta = \omega_\mathrm{d} - \omega_0$.

The Heisenberg–Langevin equations are then

$$\begin{aligned} \dot{a}_1 &= -(\kappa_a + \mathrm{i}\Delta_1) a_1 - \mathrm{i} g_1 n_1 - \mathrm{i} g_2 n_2 - \mathrm{i} f a_2 + \varepsilon_\mathrm{d} \mathrm{e}^{-\mathrm{i}\delta t} \\ &\quad + \sqrt{2\kappa_a} a_1^\mathrm{in}, \\ \dot{a}_2 &= -(\kappa_a + \mathrm{i}\Delta_2) a_2 - \mathrm{i} f a_1 - \mathrm{i} G_{au} u + \sqrt{2\kappa_a} a_2^\mathrm{in}, \\ \dot{p} &= -(\kappa_\mathrm{p} + \mathrm{i}\omega_\mathrm{p}) p - \mathrm{i} g_{np} n_2^\dagger n_2 + \sqrt{2\kappa_\mathrm{p}} p^\mathrm{in}, \\ \dot{u} &= -(\gamma_u + \mathrm{i}\Delta_u) u - \mathrm{i} G_{au} a_2 + \sqrt{2\gamma_u} u^\mathrm{in}, \\ \dot{n}_1 &= -(\kappa_{n_1} + \mathrm{i}\Delta_{n_1}) n_1 - \mathrm{i} g_1 a_1 + \sqrt{2\kappa_{n_1}} n_1^\mathrm{in}, \\ \dot{n}_2 &= -(\kappa_{n_2} + \mathrm{i}\Delta_{n_2}) n_2 - \mathrm{i} g_2 a_1 - \mathrm{i} g_{np} n_2 (p + p^\dagger) + \Omega \\ &\quad + \sqrt{2\kappa_{n_2}} n_2^\mathrm{in}. \end{aligned} \tag{3}$$

Here, κ_a, γ_u, κ_{n_r}, and κ_p are the dissipation rates of cavities, atomic ensemble, magnon modes, and phonon mode, respectively. a_r^in, p^in, u^in, and n_r^in are vacuum input noise operators with zero mean.[67] The strong drive on n_2 yields a large steady-state amplitude $|\langle n_{2s} \rangle| \gg 1$, leading also to a large cavity amplitude $|\langle a_{1s} \rangle| \gg 1$. Linearizing around the steady state, we expand operators as $\mathcal{R} = \mathcal{R}_s + \mathcal{R}_- \mathrm{e}^{-\mathrm{i}\delta t} + \mathcal{R}_+ \mathrm{e}^{\mathrm{i}\delta t}$, with $\mathcal{R} = a_1, a_2, n_1, n_2, u, p$.[68] The zero-order steady-state solutions are

$$\begin{aligned} a_{1s} &= \frac{-\mathrm{i} g_1 n_{1s} - \mathrm{i} g_2 n_{2s} - \mathrm{i} f a_{2s}}{\kappa_a + \mathrm{i}\Delta_1}, \quad a_{2s} = \frac{-\mathrm{i} f a_{1s} - \mathrm{i} G_{au} u_s}{\kappa_a + \mathrm{i}\Delta_2}, \\ p_s &= \frac{-\mathrm{i} g_{np} |n_{2s}|^2}{\kappa_\mathrm{p} + \mathrm{i}\omega_\mathrm{p}}, \quad u_s = \frac{-\mathrm{i} G_{au} a_{2s}}{\gamma_u + \mathrm{i}\Delta_u}, \\ n_{1s} &= \frac{-\mathrm{i} g_1 a_{1s}}{\kappa_{n_1} + \mathrm{i}\Delta_{n_1}}, \quad n_{2s} = \frac{\Omega - \mathrm{i} g_2 a_{1s}}{\kappa_{n_2} + \mathrm{i}\tilde{\Delta}_{n_2}}. \end{aligned} \tag{4}$$

Assuming that the coupling between the external microwave drive and the magnon mode n_2 is significantly stronger than the probe field amplitude ε_d, we solve the linearized quantum Langevin equations by considering only

the first-order perturbed solutions and neglecting higher-order terms in $\varepsilon_{\rm d}$. The cavity mode solution is then

$$a_{1-}=\varepsilon_{\rm d}\left(\mathcal{S}_1+\frac{f^2}{\mathcal{S}_{10}\mathcal{W}_6}+\frac{g_1^2}{\mathcal{S}_{12}}+\frac{g_2^2}{\mathcal{S}_2\mathcal{W}_5}\right)^{-1}, \tag{5}$$

where

$$\begin{aligned}
&\mathcal{S}_1=\kappa_a+\mathrm{i}(\Delta_1-\delta),\quad \mathcal{S}_2=\kappa_{n_2}+\mathrm{i}(\tilde{\Delta}_{n_2}-\delta),\\
&\mathcal{S}_3=\kappa_{\rm p}+\mathrm{i}(\omega_{\rm p}-\delta),\quad \mathcal{S}_4=\kappa_{\rm p}-\mathrm{i}(\omega_{\rm p}+\delta),\\
&\mathcal{X}=1-\frac{\mathcal{S}_3}{\mathcal{S}_4},\quad \mathcal{S}_5=\kappa_{n_2}-\mathrm{i}(\tilde{\Delta}_{n_2}+\delta),\\
&\mathcal{S}_6=\kappa_a-\mathrm{i}(\Delta_1+\delta),\quad \mathcal{S}_7=\kappa_a-\mathrm{i}(\Delta_2+\delta),\\
&\mathcal{S}_8=\gamma_u-\mathrm{i}(\Delta_u+\delta),\quad \mathcal{S}_9=\kappa_{n_1}-\mathrm{i}(\Delta_{n_1}+\delta),\\
&\mathcal{S}_{10}=\kappa_a+\mathrm{i}(\Delta_2-\delta),\quad \mathcal{S}_{11}=\gamma_u+\mathrm{i}(\Delta_u-\delta),\\
&\mathcal{S}_{12}=\kappa_{n_1}+\mathrm{i}(\Delta_{n_1}-\delta),\\
&\mathcal{W}_1=1+\frac{G_{au}^2}{\mathcal{S}_7\mathcal{S}_8},\quad \mathcal{W}_2=1+\frac{g_1^2}{\mathcal{S}_6\mathcal{S}_9}+\frac{f^2}{\mathcal{S}_6\mathcal{S}_7\mathcal{W}_1},\\
&\mathcal{W}_3=1+\frac{g_2^2}{\mathcal{S}_5\mathcal{S}_6\mathcal{W}_2},\quad \mathcal{W}_4=1-\frac{G_A^2\mathcal{X}}{\mathcal{S}_3\mathcal{S}_5\mathcal{W}_3},\\
&\mathcal{W}_5=1+\frac{G_A^2\mathcal{X}}{\mathcal{S}_2\mathcal{S}_3\mathcal{W}_4},\quad \mathcal{W}_6=1+\frac{G_{au}^2}{\mathcal{S}_{10}\mathcal{S}_{11}}.
\end{aligned}$$

Here, $G_A=G_{np}/\sqrt{2}$ with $G_{np}=\mathrm{i}\sqrt{2}g_{np}n_{2s}$ being the effective magnomechanical coupling. Using the standard input-output relation for cavity A,[69] the amplitude of the output field is

$$\varepsilon_{\rm out}=\frac{2\kappa_a a_{1-}}{\varepsilon_{\rm d}}. \tag{6}$$

The real part $\mathrm{Re}[\varepsilon_{\rm out}]$ corresponds to the absorption spectrum, while the imaginary part $\mathrm{Im}[\varepsilon_{\rm out}]$ corresponds to the dispersion spectrum.

The steady-state magnon amplitude n_{2s} from Eq. (4) can be written as

$$n_{2s}=\frac{\mathcal{B}\Omega}{\mathcal{B}(\kappa_{n_2}+\mathrm{i}\tilde{\Delta}_{n_2})+\mathcal{A}g_2^2(\kappa_{n_1}+\mathrm{i}\Delta_{n_1})}, \tag{7}$$

with

$$\begin{aligned}
\mathcal{A}&=(\kappa_a+\mathrm{i}\Delta_2)(\gamma_u+\mathrm{i}\Delta_u)+G_{au}^2,\\
\mathcal{B}&=\mathcal{A}(\kappa_a+\mathrm{i}\Delta_1)(\kappa_{n_1}+\mathrm{i}\Delta_{n_1})+g_1^2\mathcal{A}\\
&\quad+f^2(\gamma_u+\mathrm{i}\Delta_u)(\kappa_{n_1}+\mathrm{i}\Delta_{n_1}).
\end{aligned}$$

In Fig. 2(a), the steady-state magnon number is plotted as a function of the driving magnetic field B under different tunneling coupling strengths. The magnon number increases with B, but decreases with increasing inter-cavity coupling f for a fixed B. In Fig. 2(b), the steady-state magnon number is shown under different atom-photon coupling strengths. The magnon number decreases with increasing G_{au} when B is fixed.

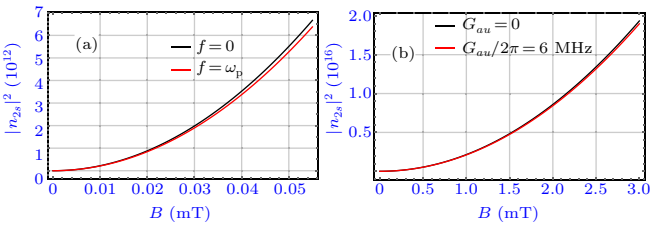


Fig. 2. Steady-state magnon number as a function of the applied magnetic field. (a) Dependence on the tunneling coupling strength f; (b) Dependence on the atom-photon coupling strength G_{au}. The magnon-cavity couplings are set as $g_1/(2\pi)=1.2$ MHz and $g_2/(2\pi)=1.2$ MHz.

3. Magnomechanically induced transparency

In this section, we numerically examine the influence of the cavity–cavity coupling strength f, atom-photon coupling strength G_{au}, and the magnetic field B on magnomechanically induced transparency within a double-cavity magnomechanical system. We utilize the effective parameters derived from recent experiments on cavity magnomechanical systems,[57,66] such as: $\omega_{1,2}/2\pi=10$ GHz, $\omega_{\rm p}/(2\pi)=10$ MHz, $\kappa_{\rm p}/(2\pi)=100$ Hz, $\omega_{n_1,n_2}/(2\pi)=10$ GHz, $\kappa_a/(2\pi)=2.1$ MHz, $\kappa_{n_1}/(2\pi)=\kappa_{n_2}/(2\pi)=0.1$ MHz, $g_1/(2\pi)=g_2/(2\pi)=1.5$ MHz, $G_{np}/(2\pi)=3.5$ MHz, $\Delta_{1,2}=\omega_{\rm p}$, $\Delta_{n_1,n_2}=\omega_{\rm p}$, and $\omega_0/(2\pi)=10$ GHz. Accordingly, the atom-cavity coupling and atomic decay rate are on the order of megahertz, with $G_{au}/(2\pi)=6$ MHz and $\gamma_u/(2\pi)=1$ MHz.[70] Moreover, the hopping rate f between the cavities is also on the order of megahertz.

In Figs. 3(a)–3(c), we display the absorption spectrum $\mathrm{Re}[\varepsilon_{\rm out}]$ of the probe field as a function of the normalized probe detuning $\delta/\omega_{\rm p}$ for different values of the cavity–cavity tunneling coupling f and the couplings g_1, g_2, and G_{np}, with the atom-cavity coupling set to zero ($G_{au}=0$). In Fig. 3(a), both the magnon-phonon coupling (G_{np}) and the magnon-photon coupling (g_1) are disabled; as a result, cavity A is coupled only to the magnon mode n_2. Under these conditions, a single transparency window appears, referred to as the MIT window. When the magnon-phonon coupling (G_{np}) is activated and g_1 remains zero, a second transparency window emerges, associated with the magnon-phonon interaction, called the MMIT window, as shown in Fig. 3(b). When g_1 is also activated, three transparency windows are observed: the single MIT window shown in Fig. 3(a) splits into a double MIT window and an MMIT window, as illustrated in Fig. 3(c). This result is consistent with Ref. [49].

We observe that the absorption peaks decrease with increasing tunneling coupling strength f, resulting in a shallower transparency window. Moreover, as f increases, the transparency window broadens and deepens. These results indicate that increasing the cavity–cavity coupling reduces absorption, enhancing the MMIT effect and, consequently, improving quantum interference. This behavior is qualitatively similar to OMIT.[71]

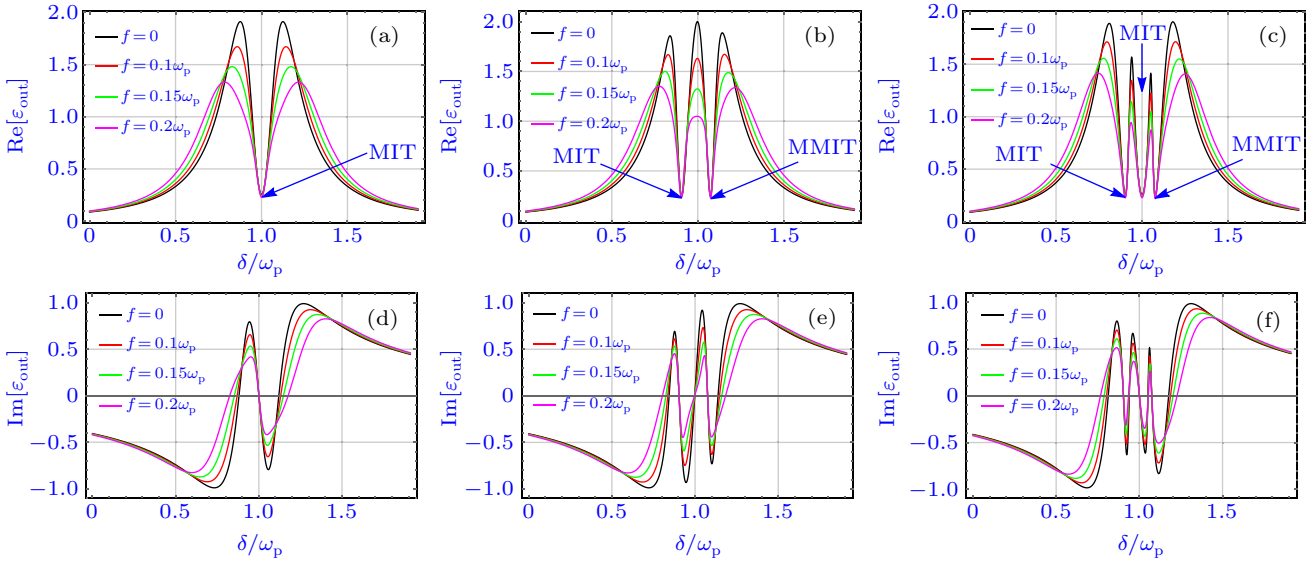


Fig. 3. Real $\mathrm{Re}[\varepsilon_{\mathrm{out}}]$ and imaginary $\mathrm{Im}[\varepsilon_{\mathrm{out}}]$ parts of the output field as a function of the normalized probe detuning $\delta/\omega_{\mathrm{p}}$ for different values of the cavity–cavity tunneling coupling strength f with $G_{au}=0$. Panels (a) and (d): $g_1=G_{np}=0$ and $g_2/(2\pi)=1.2$ MHz; panels (b) and (e): $g_1=0$ and $G_{np}/(2\pi)=g_2/(2\pi)=1.2$ MHz; panels (c) and (f): $g_1/(2\pi)=g_2/(2\pi)=G_{np}/(2\pi)=1.2$ MHz. Other parameters are the same as in the main text.

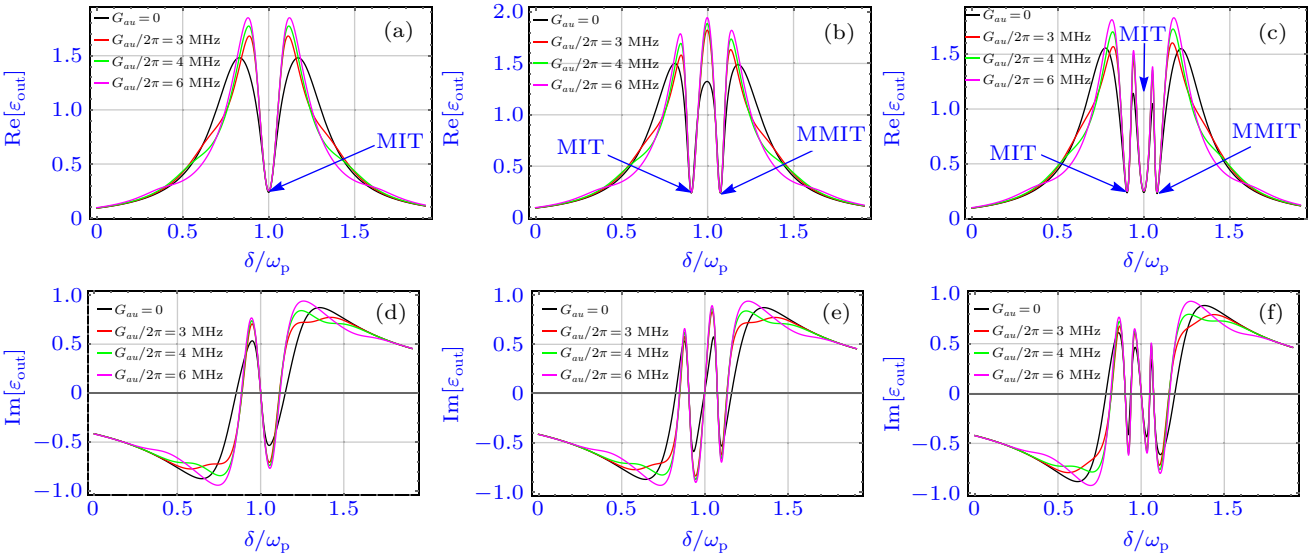


Fig. 4. Absorption and dispersion spectra of the output field as a function of the normalized probe detuning $\delta/\omega_{\mathrm{p}}$ for different values of the atom-photon coupling G_{au} with $f=0.15\,\omega_{\mathrm{p}}$. Panels (a) and (d) correspond to $g_1=G_{np}=0$ and $g_2/(2\pi)=1.2$ MHz; panels (b) and (e) correspond to $g_1=0$, $G_{np}/(2\pi)=g_2/(2\pi)=1.2$ MHz; and panels (c) and (f) correspond to $g_1/(2\pi)=g_2/(2\pi)=G_{np}/(2\pi)=1.2$ MHz. Panels (a)–(c) show the real part $\mathrm{Re}[\varepsilon_{\mathrm{out}}]$ (absorption), while panels (d)–(f) show the imaginary part $\mathrm{Im}[\varepsilon_{\mathrm{out}}]$ (dispersion). Additional parameters are given in the main text.

In Figs. 3(d)–3(f), we show the dispersion spectrum $\mathrm{Im}[\varepsilon_{\mathrm{out}}]$ of the probe field as a function of the normalized detuning $\delta/\omega_{\mathrm{p}}$ for different values of the cavity–cavity tunneling coupling f and coupling strengths g_1, g_2, and G_{np} with $G_{au}=0$. A single MIT dispersion spectrum appears when only the magnon-photon coupling (g_2) is present, as illustrated in Fig. 3(d). Figure 3(e) shows the dispersion spectrum for the case $g_1=0$, $G_{np}\neq 0$, and $g_2\neq 0$. Figure 3(f) depicts the dispersion spectrum when all three couplings are activated. It can be seen that the dispersion slope decreases with increasing tunneling coupling f, indicating that stronger tunneling enhances quantum interference and reduces the dispersion around the transparency window.

In Figs. 4(a)–4(c), we plot the absorption spectrum $\mathrm{Re}[\varepsilon_{\mathrm{out}}]$ as a function of the normalized detuning $\delta/\omega_{\mathrm{p}}$ for various values of the atom-photon coupling G_{au}, with $f=0.15\omega_{\mathrm{p}}$ and different combinations of g_1, g_2, and G_{np}. Specifically, one, two, and three transparency windows appear under the following conditions: (i) $g_1=G_{np}=0$ and $g_2\neq 0$; (ii) $g_1=0$, $G_{np}\neq 0$, and $g_2\neq 0$; and (iii) $g_1\neq 0$, $G_{np}\neq 0$, and $g_2\neq 0$, respectively. The curves corresponding to $G_{au}=0$, 3, 4, and 6 MHz are shown in black, red, green, and magenta, respectively. We note that the absorption peaks increase with larger G_{au}. Physically, a stronger atom-photon coupling enhances the interaction between cavity photons and the atomic ensemble, leading to more pronounced absorption peaks and reduced

quantum interference, consistent with Ref. [48].

Figures 4(d)–4(f) show the corresponding dispersion spectra $\mathrm{Im}[\varepsilon_{\mathrm{out}}]$ as a function of $\delta/\omega_{\mathrm{p}}$ for the same parameter sets. Figure 4(d) exhibits a single MIT dispersion spectrum in the absence of g_1 and G_{np}. Figure 4(e) corresponds to $g_1 = 0$, $G_{np} \neq 0$, and $g_2 \neq 0$, while Fig. 4(f) shows the dispersion when all three couplings are present. The results demonstrate that the dispersion slope increases with increasing G_{au}.

In Fig. 5, we depict the absorption spectrum of the probe field as a function of normalized detuning $\delta/\omega_{\mathrm{p}}$ for various values of the applied magnetic field B. Increasing B broadens the transparency windows and increases the peak separations, while shifting the windows toward lower probe frequencies. Moreover, the peak absorption decreases and the window becomes wider, eventually leading to the disappearance of the absorption feature.

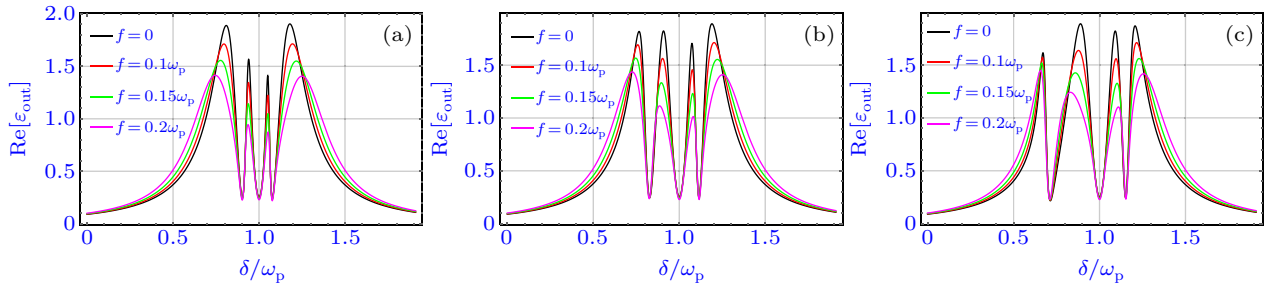


Fig. 5. Absorption spectrum $\mathrm{Re}[\varepsilon_{\mathrm{out}}]$ of the output field as a function of the normalized probe detuning $\delta/\omega_{\mathrm{p}}$ for different values of the magnetic field B and cavity-cavity tunneling strength f. Panels (a), (b), and (c) correspond to $B = 0.02$ mT, $B = 0.033$ mT, and $B = 0.05$ mT, respectively. In all panels, the magnon-phonon coupling is $g_{np}/(2\pi) = 1$ mHz, and additional parameters are given in the main text. Different curves represent $f = 0$, $0.1\,\omega_{\mathrm{p}}$, $0.15\,\omega_{\mathrm{p}}$, and $0.2\,\omega_{\mathrm{p}}$.

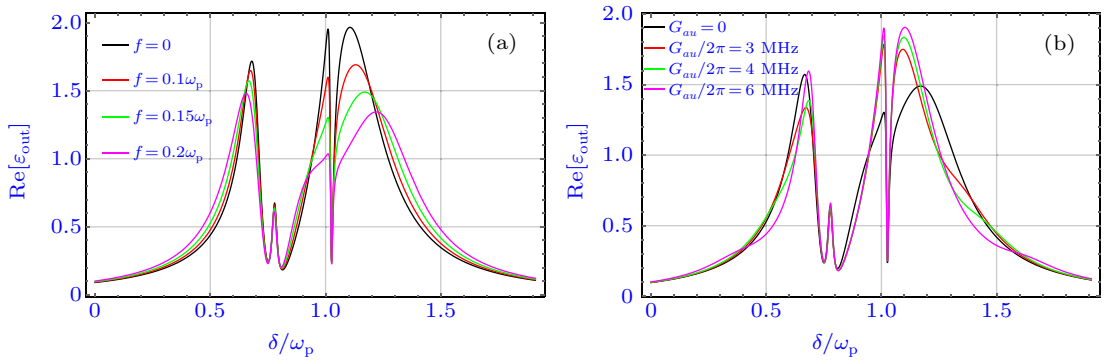


Fig. 6. Fano lineshapes in the absorption spectrum $\mathrm{Re}[\varepsilon_{\mathrm{out}}]$ of the output field as a function of normalized detuning $\delta/\omega_{\mathrm{p}}$. (a) Variation with tunneling coupling strength f, (b) Variation with atom-photon coupling G_{au}, under the non-resonant condition $\Delta_{n_{1,2}} = 0.8\,\omega_{\mathrm{p}}$. All other parameters are given in Section 3.

4. Fano resonances in the output field

In this section, we will explore the Fano resonances present in the output spectrum. The shape of the output spectrum characterized by the Fano resonance is clearly different from the symmetrical resonance curves observed in the EIT, OMIT, MIT and MMIT windows.[57,58] In systems exhibiting optomechanical-like interactions, Fano resonance arises from the existence of non-resonant interactions. In our system, this non-resonant interaction is observed as the magnon mode couples to the phonon mode via an optomechanical-like interaction, where we apply the condition $\Delta_{n_1,n_2} \neq \omega_{\mathrm{p}}$. We see in Figs. 6(a) and 6(b) asymmetrical Fano shapes with $\Delta_{n_1,n_2} \neq \omega_{\mathrm{p}}$ for different f and G_{au}, where the absorption spectrum of the output field is shown as a function of the normalized detuning $\delta/\omega_{\mathrm{p}}$. In Fig. 6(a), we have fixed the atom-photon coupling at $G_{au} = 0$. Owing to the presence of a non-resonant process $\Delta_{n_1,n_2} = 0.8\omega_{\mathrm{p}}$, the absorption spectrum evolves from a symmetric MMIT profile (Fig. 3(c)) into an asymmetric-window profile for different value of f, as illustrated in Fig. 6(a). From Fig. 6(b), in the presence of the all couplings and with the presence of the non-resonant process $\Delta_{n_1,n_2} = 0.8\omega_{\mathrm{p}}$, we observe three Fano resonances. This means that the absorption spectrum changes from a symmetrical MMIT profile (Fig. 4(c)) to an asymmetrical window profile for different G_{au}.

5. Transmission and slow/fast light

In this section, we investigate the impact of the cavity–cavity tunneling coupling f and atom-photon coupling G_{au} on the transmission and group delay of the output field. The transmission of the probe field is defined as the ratio of the amplitudes of the output field to the input field at the probe frequency, as given by the following expression:[46,72]

$$t = \frac{\varepsilon_{\mathrm{d}} - 2\kappa_a a_{1-}}{\varepsilon_{\mathrm{d}}}. \tag{8}$$

We plot in Fig. 7(a) the transmission spectrum $|t|^2$ as a

function of the normalized detuning δ/ω_p for several values of the tunneling coupling f with $G_{au}=0$. This figure shows three transparency windows when all couplings are simultaneously nonzero. The transmission peaks increase with increasing tunneling coupling f. For instance, when $f=0.15\,\omega_p$, the transmission peaks at $\delta/\omega_p\simeq 0.90$, $\delta/\omega_p\simeq 1$, and $\delta/\omega_p\simeq 1.07$ are $|t|^2=0.61$, $|t|^2=0.60$, and $|t|^2=0.63$, respectively. In contrast, for $f=0.35\,\omega_p$, the peaks are $|t|^2=0.67$, $|t|^2=0.66$, and $|t|^2=0.68$.

We plot in Fig. 7(b) the transmission spectrum $|t|^2$ versus the normalized detuning δ/ω_p for different values of the atom-photon coupling G_{au} with $f=0.15\,\omega_p$ and $g_1/(2\pi)=g_2/(2\pi)=G_{np}/(2\pi)=1.2$ MHz. The transmission peaks decrease as G_{au} increases. For example, when $G_{au}=0$, the peaks at $\delta/\omega_p\simeq 0.90$, $\delta/\omega_p\simeq 1$, and $\delta/\omega_p\simeq 1.07$ are $|t|^2=0.595$, $|t|^2=0.579$, and $|t|^2=0.616$, respectively. In contrast, for $G_{au}/(2\pi)=1.5$ MHz, the peaks reduce to $|t|^2=0.580$, $|t|^2=0.567$, and $|t|^2=0.601$.

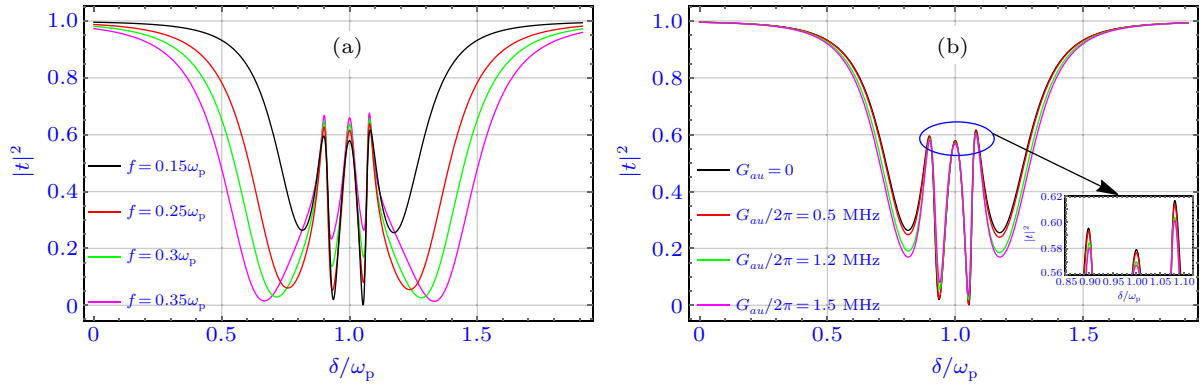


Fig. 7. (a) Plot of the transmission $|t|^2$ versus the normalized probe frequency δ/ω_p for several values of the tunneling coupling f with $G_{au}=0$ and $g_1/(2\pi)=g_2/(2\pi)=G_{np}/(2\pi)=1.2$ MHz. (b) Plot of the transmission $|t|^2$ versus the normalized probe frequency δ/ω_p for several values of the atom-photon coupling G_{au} with $f=0.15\,\omega_p$ and $g_1/(2\pi)=g_2/(2\pi)=G_{np}/(2\pi)=1.2$ MHz. The rest of the parameters are defined in Section 3.

-

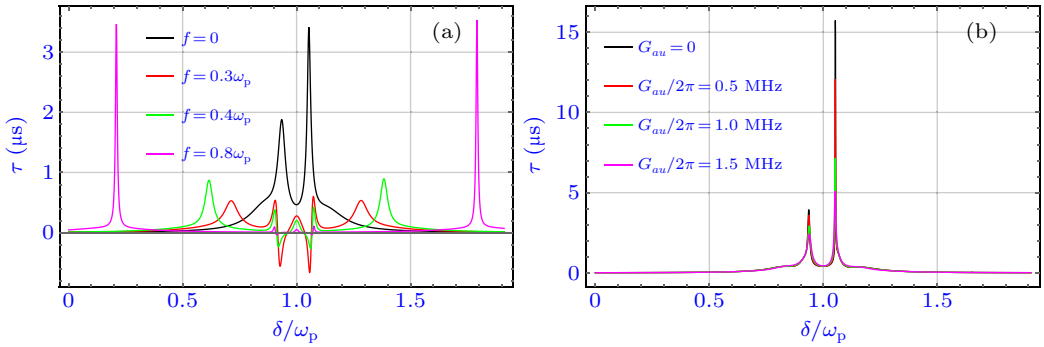


Fig. 8. Plot of the group delay τ versus the normalized detuning δ/ω_p for several values of (a) the tunneling coupling strength f with $G_{au}=0$ and $G_{sp}/(2\pi)=g_1/(2\pi)=g_2/(2\pi)=1.2$ MHz, and (b) the atom-photon coupling G_{au} with $f=0.15\,\omega_p$ and $G_{np}/(2\pi)=g_1/(2\pi)=g_2/(2\pi)=1.2$ MHz. The rest of the parameters are defined in Section 3.

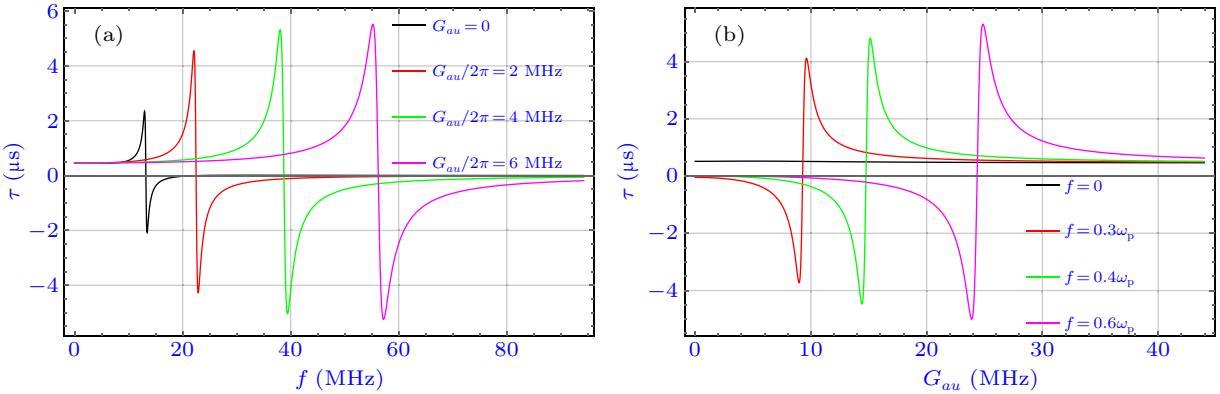


Fig. 9. Plot of the group delay τ versus (a) the tunneling coupling strength f for several values of the atom-photon coupling strength G_{au}, and (b) the atom-photon coupling G_{au} for various values of the tunneling coupling f, with $g_1=0$, $g_2/(2\pi)=1.2$ MHz, $G_{np}/(2\pi)=1.2$ MHz, and $\delta=\omega_p$. The rest of the parameters are defined in Section 3.

We define the rapid phase dispersion $\Phi = \mathrm{Arg}[t]$ within the narrow transparency window. This dispersion induces a group delay, given by[73]

$$\tau = \frac{\partial \Phi}{\partial \omega_{\mathrm{d}}} = \mathrm{Im}\left[\frac{1}{t}\frac{\partial t}{\partial \omega_{\mathrm{d}}}\right]. \tag{9}$$

A positive group delay ($\tau > 0$) indicates slow light propagation, whereas a negative group delay ($\tau < 0$) indicates fast light propagation.

Figure 8(a) shows the group delay τ as a function of the normalized detuning $\delta/\omega_{\mathrm{p}}$ for different values of the tunneling coupling f with $G_{au} = 0$ and $G_{np}/(2\pi) = g_1/(2\pi) = g_2/(2\pi) = 1.2$ MHz. We observe that when cavity A is not coupled to cavity B, i.e., $f = 0$, the group delay of the output probe field is always positive, with two peaks at $\delta = 0.93\omega_{\mathrm{p}}$ and $\delta = 1.05\omega_{\mathrm{p}}$, indicating the slow-light effect experienced by the probe field. When cavity A is coupled to cavity B, i.e., $f = 0.3\omega_{\mathrm{p}}$, a negative group delay is obtained at $\delta = 0.92\omega_{\mathrm{p}}$ and $\delta = 1.05\omega_{\mathrm{p}}$, corresponding to the fast-light effect of the output probe field. In contrast, the positive group delay at $\delta = 0.71\omega_{\mathrm{p}}$, $\delta = 0.90\omega_{\mathrm{p}}$, $\delta = \omega_{\mathrm{p}}$, and $\delta = 1.07\omega_{\mathrm{p}}$ corresponds to the slow-light effect. By increasing the tunneling coupling f, we observe an enhancement of slow light and a decrease of fast light. Therefore, the slow-light effect can be enhanced and the fast-light phenomenon suppressed by adjusting the tunneling coupling f. By comparing the transmission evolution in Fig. 7(a) with Fig. 8(a) for $f = 0.3\omega_{\mathrm{p}}$, it is evident that the peaks ($\tau > 0$) appear at $\omega_{\mathrm{d}} - \omega_0 = 0.71\omega_{\mathrm{p}}$ and $\omega_{\mathrm{d}} - \omega_0 = 1.28\omega_{\mathrm{p}}$. At these points, the transmission transitions from absorption to transmission, leading to an increase in t within this region.

In Fig. 8(b), we plot the group delay as a function of the normalized detuning $\delta/\omega_{\mathrm{p}}$ for different values of G_{au} with $f = 0.15\omega_{\mathrm{p}}$. We observe that the group delay of the output field is always positive and decreases with increasing atom-photon coupling G_{au}, indicating that only the slow-light phenomenon is observed. Comparing the transmission variation in Fig. 7(b) with the group delay in Fig. 8(b) for $G_{au}/(2\pi) = 1.5$ MHz, we find that the peaks ($\tau > 0$) occur at $\omega_{\mathrm{d}} - \omega_0 = 0.93\omega_{\mathrm{p}}$ and $\omega_{\mathrm{d}} - \omega_0 = 1.05\omega_{\mathrm{p}}$, where transmission switches from absorption to transmission. The adjustability of the group delay is attributable to the quantum interference between the probe field and the anti-Stokes field, indicating that the group delay can be dynamically tuned by regulating the cavity–cavity tunneling coupling f and the atom-photon coupling strength G_{au}.

In Fig. 9(a), we plot the group delay τ as a function of the tunneling coupling strength f for various values of the atom-photon coupling strength G_{au} with $g_1 = 0$, $g_2/(2\pi) = 1.2$ MHz, $G_{np}/(2\pi) = 1.2$ MHz, and $\delta = \omega_{\mathrm{p}}$. We observe the emergence of slow and fast light for a given value of G_{au}. For example, for $G_{au} = 0$, the group delay is positive between $f = 0$ and $f = 13.20$ MHz, and negative between $f = 13.20$ MHz and $f = 21.09$ MHz. Additionally, the maximum group delay can be increased by adjusting G_{au}, with higher values of the atom-photon coupling leading to larger group delays.

Figure 9(b) shows the group delay τ as a function of atom-photon coupling strength G_{au} for different values of the tunneling coupling strength f, with $g_1 = 0$, $g_2/(2\pi) = 1.2$ MHz, $G_{np}/(2\pi) = 1.2$ MHz, and $\delta = \omega_{\mathrm{p}}$. When cavity A is not coupled to cavity B, i.e., $f = 0$, the group delay is positive and fixed at $\tau = 0.5$ μs. Conversely, when the tunneling coupling is present, i.e., $f = 0.3\omega_{\mathrm{p}}$, the group delay exhibits two regions: a negative region between $G_{au} = 0$ and $G_{au} = 9.27$ MHz, indicating fast light, and a positive region for $G_{au} > 9.27$ MHz, indicating slow light. We note that the group delay τ increases significantly with the tunneling coupling strength f. The group delay is proportional to the slope of the dispersion curve in the transparency region (see Fig. 3(f)). As f increases, the slope becomes steeper due to enhanced coupling and interference between the two optical cavities, resulting in slower propagation of the probe field, corresponding to the slow-light effect.

6. Feasibility

The feasibility of the proposed double-cavity magnomechanical system is supported not only by previously demonstrated subsystems but also by the realistic choice of parameters used in our numerical analysis. The system parameters are taken from recent experimental reports on cavity magnomechanical platforms.[57,66,70] Specifically, the cavity and magnon mode frequencies are $\omega_{1,2}/(2\pi) = \omega_{n_1,n_2}/(2\pi) = 10$ GHz, while the mechanical frequency is $\omega_{\mathrm{p}}/(2\pi) = 10$ MHz. The corresponding decay rates are $\kappa_a/(2\pi) = 2.1$ MHz, $\kappa_{n_1,n_2}/(2\pi) = 0.1$ MHz, and $\kappa_{\mathrm{p}}/(2\pi) = 100$ Hz, all within experimentally accessible values.[49] The single-photon magnomechanical couplings $g_{1,2}/(2\pi) = 1.5$ MHz and the enhanced coupling $G_{np}/(2\pi) = 3.5$ MHz have been experimentally achieved in hybrid cavity-magnon systems.[57] The atom-photon coupling $G_{au}/(2\pi) = 6$ MHz and atomic decay rate $\gamma_u/(2\pi) = 1$ MHz are also within the typical range of cavity quantum electrodynamics experiments.[70] Furthermore, the inter-cavity coupling rate f is assumed to be on the order of megahertz, which has been demonstrated in coupled cavity experiments. Therefore, all parameters employed in our theoretical calculations are within experimentally realistic ranges, confirming the feasibility of realizing the proposed magnomechanical-induced transparency phenomenon with current technologies.

7. Conclusion

In conclusion, we have examined the absorption, dispersion, and transmission spectra of a hybrid magnomechanical system. MMIT and MIT can be identified in the absorption and transmission spectra as a result of photon-magnon and phonon-magnon interactions. The cavity–cavity tunneling coupling has the potential to enhance MIT and MMIT. Subsequently, we investigated the impact of the atom-photon coupling on the absorption and transmission spectra. The results indicate that the transparency windows decrease when the atom-photon coupling is increased. We also studied the influence of the magnetic field on the absorption spectrum. Additionally, the presence of anti-Stokes processes in the system gives rise to the Fano resonance phenomenon, which is thoroughly examined. We have studied the conditions for slow and fast light propagation in our system, which can be regulated by various system parameters. It was demonstrated that the tunability of the tunneling coupling and atom-photon coupling has a significant impact on the slow- and fast-light phenomena in our magnomechanical system.

Acknowledgment

M. Amghar expresses gratitude for the financial support received from the National Center for Scientific and Technical Research (CNRST) under the PhD-Associate Scholarship (PASS) program.

References

[1] Harris S E 1997 *Phys. Today* **50** 36
[2] Harris S E, Field J E and Imamoglu A 1990 *Phys. Rev. Lett.* **64** 1107
[3] Boller K J, Imamoglu A and Harris S E 1991 *Phys. Rev. Lett.* **66** 2593
[4] Fleischhauer M, Imamoglu A and Marangos J P 2005 *Rev. Mod. Phys.* **77** 633
[5] Lvovsky A I, Sanders B C and Tittel W 2009 *Nat. Photonics* **3** 706
[6] Fleischhauer M and Lukin M D 2002 *Phys. Rev. A* **65** 022314
[7] Kocharovskaya O, Rostovtsev Y and Scully M O 2001 *Phys. Rev. Lett.* **86** 628
[8] Turukhin A V, Sudarshanam V S, Shahriar M S, Musser J A, Ham B S and Hemmer P R 2001 *Phys. Rev. Lett.* **88** 023602
[9] Jain M, Xia H, Yin G Y, Merriam A J and Harris S E 1996 *Phys. Rev. Lett.* **77** 4326
[10] Weis S, Riviere R, Deleglise S, Gavartin E, Arcizet O, Schliesser A and Kippenberg T J 2010 *Science* **330** 1520
[11] Shen J Q and He S 2006 *Phys. Rev. A* **74** 063831
[12] Chang Y and Sun C P 2011 *Phys. Rev. A* **83** 053834
[13] Paspalakis E and Knight P L 2002 *Phys. Rev. A* **66** 015802
[14] Diniz E C, Borges H S and Villas-Boas C J 2018 *Phys. Rev. A* **97** 043848
[15] Yang X D, Yu M B, Kwong D L and Wong C W 2009 *Phys. Rev. Lett.* **102** 173902
[16] Luo X Q, Wang D L, Zhang Z Q, Ding J W and Liu W M 2011 *Phys. Rev. A* **84** 033803
[17] Patnaik A K, Liang J Q and Hakuta K 2002 *Phys. Rev. A* **66** 063808
[18] Aspelmeyer M, Kippenberg T J and Marquardt F 2014 *Rev. Mod. Phys.* **86** 1391
[19] Teufel J D, Li D, Allman M S, Cicak K, Sirois A J, Whittaker J D and Simmonds R W 2011 *Nature* **471** 204
[20] Agarwal G S and Huang S 2012 *Phys. Rev. A* **85** 021801
[21] Zhang J Q, Li Y, Feng M and Xu Y 2012 *Phys. Rev. A* **86** 053806
[22] Huang S M and Agarwal G S 2010 *Phys. Rev. A* **81** 033830
[23] Li X Y, Nie W J, Chen A X and Lan Y H 2018 *Phys. Rev. A* **98** 053848
[24] Wu S C, Qin L G, Jing J, Yan T M and Lu J 2018 *Phys. Rev. A* **98** 013807
[25] Amazioug M, Daoud M, Singh S K and Asjad M 2023 *Quantum Inf. Process.* **22** 301
[26] Han Y, Cheng J and Zhou L 2011 *J. Phys. B: At. Mol. Opt. Phys.* **44** 165505
[27] Tesfahannes T G 2021 *Quantum Inf. Process.* **20** 116
[28] Abdi M and Plenio M B 2019 *Phys. Rev. Lett.* **122** 023602
[29] Asjad M 2013 *J. Russ. Laser Res.* **34** 159
[30] Shahidani S, Naderi M H and Soltanolkotabi M 2013 *Phys. Rev. A* **88** 053813
[31] Huebl H, Zollitsch C W, Lotze J, Hocke F, Greifenstein M, Marx A, Gross R and Goennenwein S T 2013 *Phys. Rev. Lett.* **111** 127003
[32] Zhang X F, Zou C L, Jiang L and Tang H X 2014 *Phys. Rev. Lett.* **113** 156401
[33] Tabuchi Y, Ishino S, Ishikawa T, Yamazaki R, Usami K and Nakamura Y 2014 *Phys. Rev. Lett.* **113** 083603
[34] Bai L, Harder M, Chen Y P, Fan X, Xiao J Q and Hu C M 2015 *Phys. Rev. Lett.* **114** 227201
[35] Goryachev M, Farr W G, Creedon D L, Fan Y H, Kostylev M and Tobar M E 2014 *Phys. Rev. Appl.* **2** 054002
[36] Zhang D, Wang X M, Li T F, Luo X Q, Wu W D, Nori F and You J Q 2015 *npj Quantum Inf.* **1** 15014
[37] Soykal O O and Flatt M E 2010 *Phys. Rev. Lett.* **104** 077202
[38] Zhang X, Zhu N, Zou C L and Tang H X 2016 *Phys. Rev. Lett.* **117** 123605
[39] Tabuchi Y, Ishino S, Noguchi A, Ishikawa T, Yamazaki R, Usami K and Nakamura Y 2015 *Science* **349** 405
[40] Potts C A, Varga E, Bittencourt V A, Kusminskiy S V and Davis J P 2021 *Phys. Rev. X* **11** 031053
[41] Yang Z X, Wang L, Liu Y M, Wang D Y, Bai C H, Zhang S and Wang H F 2020 *Front. Phys.* **15** 52504
[42] Chabar N, Amghar M and Amazioug M 2024 *Phys. Lett. A* **519** 129712
[43] Amghar M and Amazioug M 2024 *Optik* **311** 171940
[44] Amazioug M, Teklu B and Asjad M 2023 *Sci. Rep.* **13** 3833
[45] Li J and Zhu S Y 2019 *New J. Phys.* **21** 085001
[46] Amghar M, Chabar N and Amazioug M 2024 *Chin. Phys. B* **33** 120308
[47] Amghar M, Chabar N and Amazioug M 2024 *J. Opt. Soc. Am. B* **42** 120
[48] Liao Q, Peng K and Qiu H 2023 *Chin. Phys. B* **32** 054205
[49] Ullah K, Naseem M T and Müstecaplıoğlu Ö E 2020 *Phys. Rev. A* **102** 033721
[50] Lu H, Wang C Q, Yang L and Jing H 2018 *Phys. Rev. Appl.* **10** 014006
[51] Sohail A, Arif R, Akhtar N, Ziauddin, Peng J X, Xianlong G and Gu Z 2023 *Eur. Phys. J. Plus* **138** 417
[52] Sohail A, Ahmed R and Ali H 2024 arXiv:2405.09845 [quant-ph]
[53] Shen R C, Li J, Fan Z Y, Wang Y P and You J Q 2022 *Phys. Rev. Lett.* **129** 123601
[54] Wang Y P, Zhang G Q, Zhang D K, Li T F, Hu C M and You J Q 2018 *Phys. Rev. Lett.* **120** 057202
[55] Diederich G M, Cenker J, Ren Y, Fonseca J, Chica D G, Bae Y J, Zhu X, Roy X, Cao T, Xiao D and Xu X 2023 *Nat. Nanotechnol.* **18** 23
[56] Fano U 1961 *Phys. Rev.* **124** 1866
[57] Zhang X, Zou C L, Jiang L and Tang H X 2016 *Sci. Adv.* **2** e1501286
[58] Qu K and Agarwal G S 2013 *Phys. Rev. A* **87** 063813
[59] Liu Z Q, Liu L, Meng Z Z, Tan L and Liu W M 2023 *Opt. Express* **32** 722
[60] Bai C H, Wang D Y, Wang H F, Zhu A D and Zhang S 2016 *Sci. Rep.* **6** 33404
[61] Chen B, Shang L, Wang X F, Chen J B, Xue H B, Liu X and Zhang J 2019 *Phys. Rev. A* **99** 063810
[62] Holstein T and Primakoff H 1940 *Phys. Rev.* **58** 1098
[63] Hammerer K, Sørensen A S and Polzik E S 2010 *Rev. Mod. Phys.* **82** 1041
[64] Zheng S B 2012 *Phys. Rev. A* **86** 013828
[65] Genes C, Vitali D and Tombesi P 2008 *Phys. Rev. A* **77** 050307
[66] Li J, Zhu S Y and Agarwal G S 2018 *Phys. Rev. Lett.* **121** 203601
[67] Xiong H and Wu Y 2018 *Appl. Phys. Rev.* **5** 011303
[68] Huang S and Agarwal G S 2011 *Phys. Rev. A* **83** 043826
[69] Walls D and Milburn G 2007 *Quantum Optics* pp. 30–49 (Berlin: Springer)
[70] Dilawaiz, Qamar S and Irfan M 2024 *Phys. Rev. A* **109** 043708
[71] Liao Q, Xiao X, Nie W and Zhou N 2020 *Opt. Express* **28** 5288
[72] Amghar M and Amazioug M 2024 *Int. J. Quantum Inf.* **22** 2450043
[73] Tarhan D, Huang S and Müstecaplıoğlu Ö E 2013 *Phys. Rev. A* **87** 013824